Hindawi
Journal of Sensors
Volume 2022, Article ID 6856784, 23 pages
https://doi.org/10.1155/2022/6856784

Research Article

Comparative Assessment and Experimental Validation of a Prototype Phase-Optical Time-Domain Reflectometer for Distributed Structural Health Monitoring

Massimo Leonardo Filograno,[1,2] George Piniotis,[3] Vassilis Gikas,[3] Vasileios Papavasileiou,[4] Charis J. Gantes,[4] Maria Kandyla,[1] and Christos Riziotis[1,5]

[1]*National Hellenic Research Foundation, Theoretical and Physical Chemistry Institute, Athens 11635, Greece*
[2]*Department of Electrical and Electronic Engineering, University of Jeddah, Jeddah 23890, Saudi Arabia*
[3]*School of Rural, Surveying and Geoinformatics Engineering, National Technical University of Athens, Zographos, 15780 Athens, Greece*
[4]*School of Civil Engineering, National Technical University of Athens, Zographos, 15780 Athens, Greece*
[5]*Defence and Security Research Institute, University of Nicosia, Nicosia CY-2417, Cyprus*

Correspondence should be addressed to Maria Kandyla; kandyla@eie.gr and Christos Riziotis; riziotis@eie.gr

Received 23 December 2021; Accepted 25 January 2022; Published 23 March 2022

Academic Editor: Carlos Marques

Dynamic characterization and Structural Health Monitoring (SHM) are crucial tools, of increasing demand, for reliable operation and predictive maintenance of large infrastructures, as the percentage of critically ageing infrastructures is growing steadily. We present a minimally invasive and synchronous fiber optic monitoring system for SHM, based on Phase-Optical Time-Domain Reflectometry (Phase-OTDR), and we assess its applicability and performance on a modular Bailey-type bridge of 1 : 2.5 scale. Phase-OTDR systems, along with other fiberoptic-distributed techniques have proven their capabilities in long-range SHM applications, although their complexity and high cost limits drastically their applicability and SHM market penetration. Here, we propose the use of a prototype Phase-OTDR system, featuring customized interrogation instrumentation with a balanced trade-off between performance and cost. Its experimental validation is achieved by comparison with well-established commercial monitoring systems, such as Ground-Based Radar Interferometer (GBRI), laser tracker, and multipoint optical Fiber Bragg Gratings (FBGs), in various excitation conditions and structure-damage scenarios, easily implementable in the model bridge. Finite-element modelling (FEM) and simulations were employed to study the bridge behaviour and provide a reference and comparison framework for the experimental characterization. The Phase-OTDR system successfully detected the structural behaviour in an efficient distributed manner, demonstrating comparable performance to commercial point sensor systems, thus demonstrating its application potential.

1. Introduction

1.1. Ageing Control of Structures. Ageing civil infrastructure is likely to experience deterioration of strength and stiffness, due to a wide variety of natural and man-made causes. Natural aspects may be environmental, such as temperature variations, freeze-thaw cycles, exposure to humidity, cycles of wind, and wave pressures. Those effects are gradually accumulated over time, but they may be more abrupt, with earthquakes, tornados, and tsunamis being the major occurrences. Examples of man-made adverse actions are environmental pollution, blasts, and vehicle and vessel collisions. With steel and reinforced concrete being the two most widely used structural materials worldwide, damage and wear of steel structures are primarily manifested by corrosion and fatigue cracking, while of concrete structures by cracking and spalling of the cover and corrosion of the reinforcement. Considering the nominal design life of most structures is 50

years, and of particularly important structures 100 years, it is evident that a large percentage of the built environment is approaching or has even exceeded its nominal lifetime. Therefore, in the coming years, maintenance and rehabilitation will play an increasingly important role compared to the design of new structures.

Predictive maintenance of civil engineering structures is an expensive task, the importance of which is too often underestimated. Manual and periodic inspections of large structures, such as bridges, are crucial for proper maintenance. Nevertheless, such controls are time-consuming and can only provide evidence of progressive deterioration of a bridge condition, provided it is visible by direct eye inspection [1, 2]. In addition, static load testing is traditionally used to assess the actual load capacity of a bridge against the numerical analysis obtained at the design stage [3]. However, load testing alone cannot reveal the dynamic response of a bridge and the changes that might occur in its dynamic features (such as variations in the modal characteristics), which act as precursors of damage evidence in the future. Therefore, in the case of large bridge structures, for continuous monitoring of their static and dynamic characteristics, it is necessary to reveal their "*health status*" and assist in taking preventive measures to ensure safe and cost-effective operation [4–6].

Inevitably, the number of structures, especially bridges, which need continuous monitoring is increasing with time, including a number of cases that collapse, sometimes with a long list of fatalities [7]. Notably, in order to prevent further casualties, even collapsed structures require real-time, continuous monitoring until demolition is completed. Currently, commercial technologies are not entirely suitable for this purpose. Traditionally, engineering surveying techniques and experimental mechanics technologies, such as robotic stations, inclinometers, extensometers, and accelerometers, are used in Structural Health Monitoring (SHM) [8–13]. More recently, new technologies based on Global Navigation Satellite System (GNSS) [14–16], radar [17], and image correlation [18] principles have also been extensively adopted. In addition to these, a distinct, rapidly expanding technology used in SHM is strain gauges. They rely either on electrical transduction or on optical interactions, such as optical fiber sensors. Sensors based on electrical transduction are technologically mature, relatively low-cost, and accurate. However, electrical sensors are sensitive to electromagnetic noise, due to the fact that the sensing location is most often unprotected, and they require multiplexing and communication networks to allow remote sensing of several points. Sensors based on optical transduction are potentially more accurate and sensitive, but only some of them can be considered industrially mature. The most widely applied, cost-effective, and the most accessible SHM optical sensors are Fiber Bragg Gratings (FBGs), well known as optical strain gauges, which are point sensors providing strain measurements at specific locations [19–21]. There are also alternative photonic sensing approaches [22] and several other optical technologies, such as displacement interferometers, electric current sensors, accelerometers, and gyroscopes, some of which provide distributed sensing, interrogating at once the entire structure, but their application is still not established due to prohibitive costs.

In this work, we present the operational characteristics of a distributed optical fiber-sensing technology, Phase-Optical Time-Domain Reflectometry (Phase-OTDR) operated by a low-cost interrogator, custom developed to meet the needs of SHM applications. We validate the operation and specifications of the system in a model structure (a bridge), by comparing it with three well-established technologies, namely, FBGs, Ground-Based Radar Interferometry (GBRI), and Laser Tracking. The crucial advantage provided by the Phase-OTDR system is the lower cost per sensed point, compared to the other established sensing technologies. Preliminary results of this application of the Phase-OTDR system have been reported previously in Ref. [23] as an unreviewed conference proceeding paper.

1.2. Distributed Monitoring Methods. Optical fiber sensors can be classified as point or distributed. The latter can monitor several thousand points simultaneously, providing a significantly reduced cost per sensed point; however, depending on the specific technology and performance requirements, their total cost can be particularly high. The operational principles of distributed optical fiber sensors can be based on Rayleigh, Raman, or Brillouin scattering effects [24, 25]. The most suitable distributed technologies for real-time SHM of structure vibrations are considered those based on Rayleigh and Brillouin scattering, while Raman-based sensors are commercially available for temperature monitoring [20, 26]. One subcategory of Rayleigh sensors is Phase-OTDR, which are emerging as competitive distributed acoustic sensors [27, 28]. Reflectometry techniques in general include optical low-coherence reflectometry (OLCR), optical time-domain reflectometry (OTDR), and optical frequency domain reflectometry (OFDR). OLCR shows high spatial resolution and reduced sensing range (order of meters). OFDR and OTDR are twin techniques, in which the information is encoded and decoded in the frequency and time domain of the scattered signal, respectively. Typically, OFDR has better spatial resolution, while OTDR has bigger sensing range (tens to hundreds of km) [24]. Phase-OTDR systems retrieve information on the state of the optical fiber (due to strain or temperature conditions) through the amplitude of the retrieved Rayleigh backscattered signal, the changes of which reflect changes in the optical fiber and hence in the sensed structure on which the fiber is attached. For such systems, the relation between strain (or temperature) and the backscattered signal is linear only at low levels of perturbations [29]. Typical simplified Phase-OTDR systems do not have countermeasures to avoid nonlinearities; therefore, their use is limited in locating the position of a perturbation and its frequency pattern [30]. Instead, more sophisticated linear setups can measure accurately strain and temperature along the entire sensing range. This last Phase-OTDR category, which employs techniques such as coherent detection [31] and chirped pulses [32], can reveal fast perturbations with high accuracy [33], allowing a direct comparison with well-established point-sensing technologies.

The specific nonlinear Phase-OTDR system presented here is the result of a compromise between performance and cost, using commercial components, specifically combined and tuned for SHM applications, with a cost under 10 k€, which is substantially lower than the cost of typical commercial linear Phase-OTDR systems [34]. We present monitoring tests of the system on a scaled Bailey-type steel bridge model, which we also monitor with FBGs, GBRI, and Laser Tracking. Although the model bridge is not the ideal test case for the proposed Phase-OTDR system, due to its limited total length (6.12 m), it provides the necessary framework and a fully controllable laboratory environment for simultaneous employment of four distinct monitoring approaches (Laser Tracking, GBRI, FBG, Phase-OTDR) under specific excitation conditions. In a real application example of km-length bridges or other infrastructures, the employment of Laser Tracking or GBRI would not be possible on this length scale. Here, the access to various monitoring systems can provide a rigorous assessment of the bridge state and comparative characterization of the newly introduced Phase-OTDR system performance.

2. Materials and Methods

2.1. The Scaled Bailey-Type Steel Bridge. Bailey bridges are through-type truss bridges, which are built on-site from a preengineered system of ready-to-assemble components. The roadway is carried between two main girders, each of which is formed from panels, pinned end-to-end. The different arrangements of panels are known as *trusses* and *storeys*, and there are seven types of Bailey bridge configurations, depending on the number of *trusses* and *storeys*. The scaled model in this study is based on a Bailey bridge, single-truss and single-storey (one truss made of five panels and one storey at each girder) [35]. Each main girder is composed of five prewelded typical panels, which are joined together using pins through predrilled holes in the lugs of the upper and lower chords of the panels. The hybrid frame/truss structural system also constitutes the bridge safety barriers. Figure 1(a) shows a schematic view of the bridge model employed in this study. Transoms are clamped on the top flange of the bottom chords of the panels with transom clamps, and they extend outwards in an overhanging arrangement. The lateral stability of the main girders is ensured with inclined rakers connecting the vertical posts of the panels to the overhanging cantilever parts of the transoms. In order to ensure diaphragm action of the deck and overall lateral stability, horizontal sway braces are arranged between the girders, below the transoms. In order to facilitate quick construction, which is necessary for this type of bridges, eccentricities are encountered at the connections between transoms, diagonal rods of sway braces and girder posts, although this is not optimum from the structural point of view.

In order to investigate the dynamic behaviour of such bridges in a controlled environment, a 15.3 m long physical model has been constructed in a 1 : 2.5 scale, in accordance to similitude law. The basic scaled model dimensions are shown in Figure 1(b). The scaled model has a 6125 mm span with a 1815 mm wide deck and a total width (including transoms) of 2400 mm, while the panel height is 582 mm. Each panel has dimensions of 1225 mm by 582 mm (Figure 1(c)).

In accordance to the similitude law, similarity in inertial properties of upper and lower panel chords is achieved, and their cross-section type (back to back UPN sections) is maintained, as these members are the most critical for the dynamic behavior of the bridge. For diagonal and vertical members of main girders, similarity of their cross-sectional area is ensured, considering that these members have mainly axial action. The upper and lower chords of each panel have built-up sections, consisting of two back to back UPN 30×15 sections, the vertical and diagonal members have square hollow cross-section $20 \times 20 \times 2$, and the transom has an IPN80 cross-section, while for sway braces, Ø8 rods are used. For all members, S235 structural steel is used.

2.2. The Excitation Source. The vibration excitation source used in this study is a linear motor (shaker) that allows the generation of controlled, arbitrary waveforms. The apparatus used in the tests is the Modal 110 exciter (MB Dynamics Inc.), the main characteristics of which are as follows:

(i) Maximum force: 500 N

(ii) Bandwidth: DC-5000 Hz

(iii) Max acceleration: 830 m/s^2 peak

(iv) Max velocity: 1.6 m/s peak

(v) Weight: 25 kg

The shaker was mounted firmly on the floor using screws with finery bypass (Figure 2) and remained fixed at the same location throughout the entire testing process. Its absolute location is at 418.8 cm on the south side of the bridge.

A LabView® application was generated to process in real-time the incoming signals to the shaker through a power amplifier. The excitations provided to the bridge by the shaker were single harmonic (one vibration frequency), harmonic sweeps, shocks, and white noise excitations.

2.3. Ground-Based Radar Interferometer (GBRI) Sensor. GBRI technology allows the computation of scattering object displacements using the phase variation information obtained by a radar sensor from repeated electromagnetic pulse transmissions. GBRI has been proven a suitable technology for dynamic monitoring of large civil engineering structures. This is due to its ultrahigh accuracy capability in displacement measurements (up to 0.1 mm in field conditions), its high sampling frequency (up to 20 Hz), and long observation distances (>500 m). The GBRI system used in this work is the IBIS-S (Image By Interferometric Survey of Structures) system produced by IDS GeoRadar® (Ingegneria Dei Sistemi, Pisa, Italy). This sensor implements two well-known radar techniques—i.e., the Interferometric technique and the Stepped-Frequency Continuous Wave technique, which allow simultaneous monitoring of several targets placed at different distances from the radar sensor [36]. Despite its inability to distinguish targets placed at the same

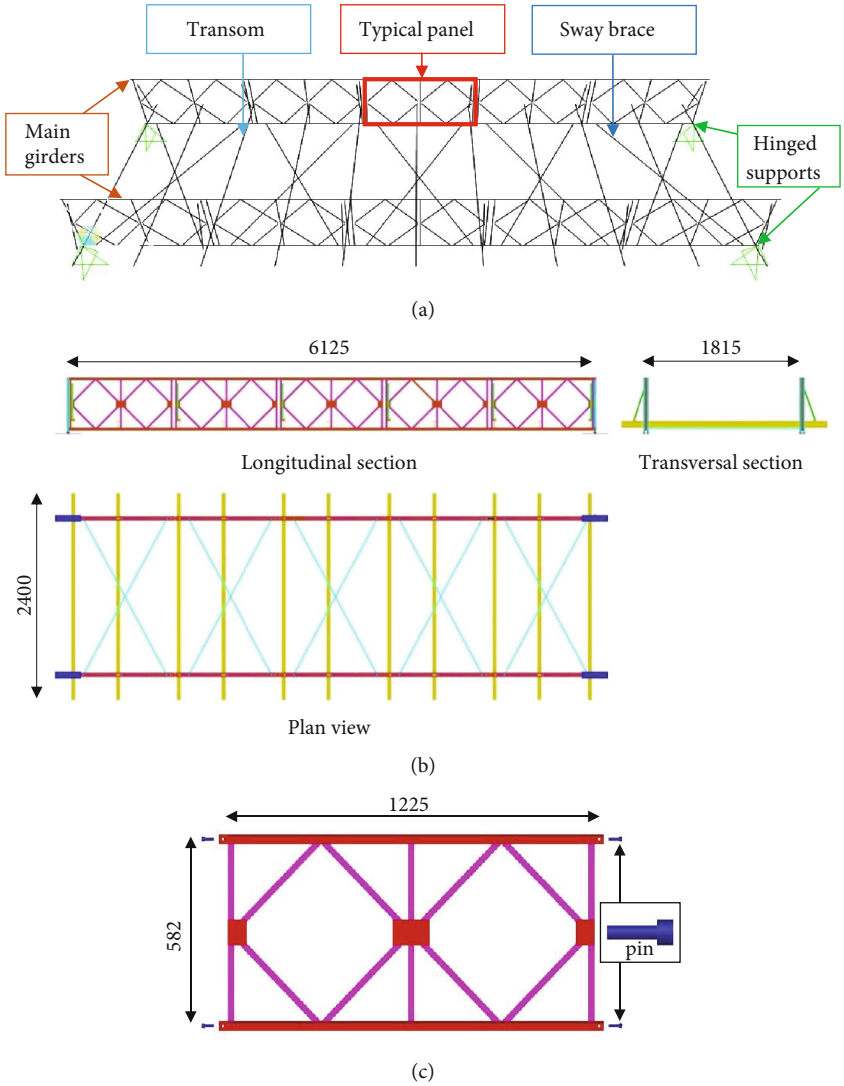

Figure 1: (a) Typical Bailey bridge and names of basic components. (b) Dimensions of scaled Bailey bridge model in mm. (c) The typical panel of scaled Bailey bridge model.

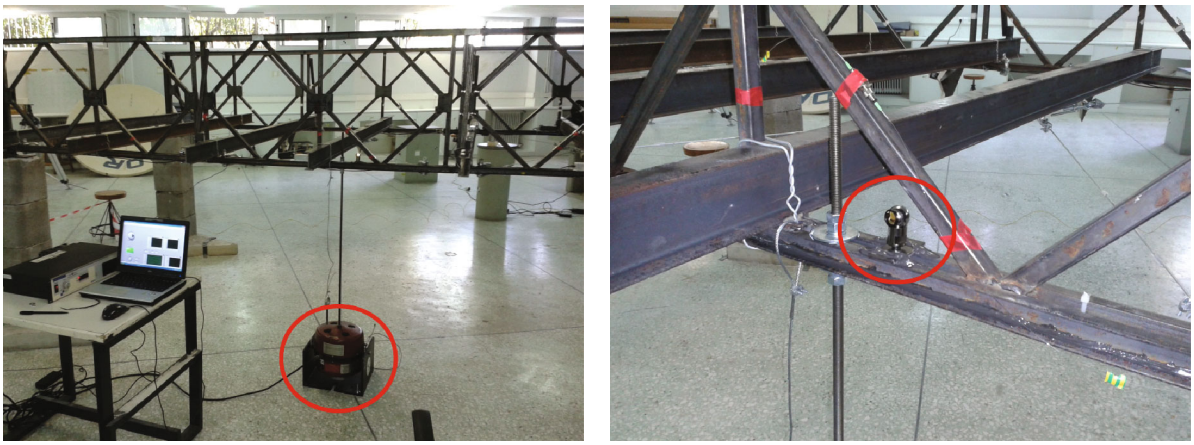

(a) (b)

Figure 2: View of the shaker apparatus (a); detail of the bridge element that received the excitation (b). The laser tracker retroreflector is shown on the right, next to the circled junction.

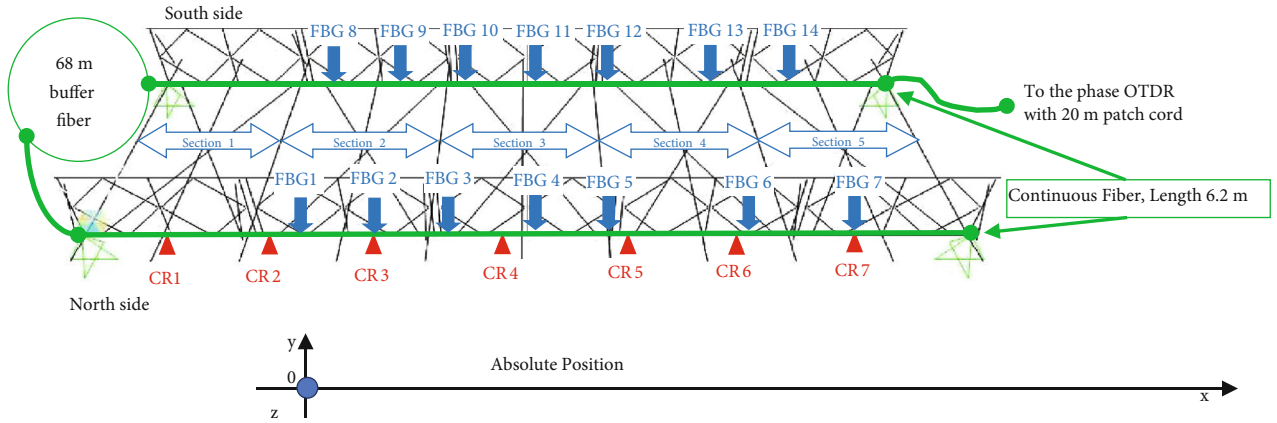

Figure 3: The 7 CR and 14 FBG point sensor locations and the continuous fiber (Phase-OTDR system), which senses both sides of the scaled Bailey bridge model.

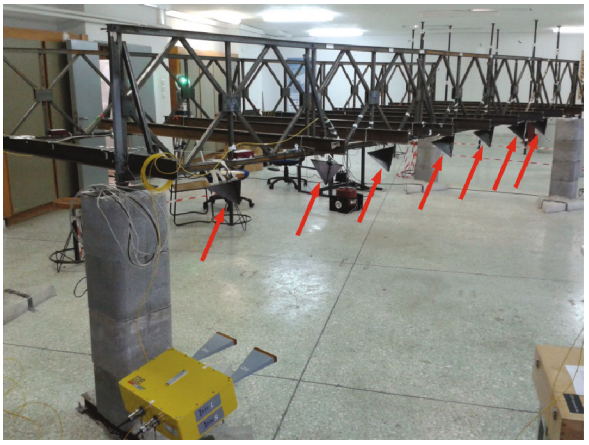

Figure 4: Picture of the installed GBRI system and the 7 CRs in the laboratory (indicated by the arrows).

Table 1: Absolute positions of FBGs.

FBG number	Bridge section	Position	Bridge side	Absolute position (cm)
1	2	Section	North	152.8
2	2	Section	North	202
3	2-3	Junction	North	245
4	3	Section	North	307.5
5	4-5	Junction	North	368.4
6	4	Section	North	460.2
7	5	Section	North	512
8	2	Section	South	152.8
9	2	Section	South	202
10	2-3	Junction	South	245
11	3	Section	South	307.5
12	4-5	Junction	South	368.4
13	4	Section	South	460.2
14	5	Section	South	512

observation distance, IBIS-S has been extensively used for the dynamic testing of civil structures (e.g., bridges, buildings, and chimneys) and has become a well-established technique for nondestructive evaluation and SHM. Usual environmental factors affecting the GBRI performance, such as humidity, temperature, and pressure, were negligible in this indoors study, where short (<15 min) acquisition durations and relatively short (<200 m) observation distances were employed [37, 38]. On the other hand, a confined laboratory environment may cause signal multipath effects. However, in this work, the relatively ample size of the lab room resulted in negligible multipath effects. In any case, multipath effects would affect only the amplitude of the observed displacements, leaving their vibration pattern and frequency content unaffected, as has been proven by extensive indoor and outdoor testing.

Figure 3 shows the location of the corner reflectors (CR) mounted on the north side of the bridge as follows: CR1 at 61 cm, CR2 at 141 cm, CR3 at 202 cm, CR4 at 293 cm, CR5 at 375 cm, CR6 at 452.2 cm, and CR7 at 512 cm. Also, Figure 4 shows a picture of the sensor and CR target observation geometry GBRI in the laboratory. The CRs were mounted on the north side of the bridge because the main structural elements of bridges of this type are the frames on the two opposite sides. The members of these frames, particularly their upper and lower chords, are the ones where the maximum response is obtained. Equivalently, they could have been mounted on the south side of the bridge but not on the members below the bridge because they have a local function and would have not been representative. In order to achieve the optimal reflection scenario of the emitted GBRI signal, the GBRI sensor was placed below the level of the bridge deck and adjacent to one of the bridge-supporting pillars so that a radial observation geometry was reconstructed towards the CRs. The CRs were mounted below and along the lower chord of the north frame of the bridge deck to allow a clear observation view at locations of maximum expected displacement. Following extensive testing, the foregoing observation scenario proved to be

Figure 5: An FBG (circled) attached between the continuous Phase-OTDR fiber (top) and a corner reflector (bottom).

optimal facilitating adequate signal reflection from all targets and satisfactory Signal-to-Noise-Ratio (SNR) values according to the system specifications.

2.4. Photonic Sensors: FBGs and Phase-OTDR

2.4.1. Fiber Bragg Gratings (FBGs). FBGs are narrow-linewidth optical fiber filters, the reflected wavelength of which depends on the strain and temperature changes applied to the fiber. FBG interrogators detect wavelength shifts, which are converted to strain values, assuming structures with constant temperature, by the following equation [39, 40]:

$$\Delta\lambda_B = K_\varepsilon \varepsilon, \tag{1}$$

where ε is the strain and K_ε is the strain constant, characteristic of the FBG, the value of which is usually ~1.2 pm/$\mu\varepsilon$.

In this work, we used a commercial 4-channel FBG interrogator (MicronOptics SM130, Atlanta, GA 30345, United States), which allows simultaneous monitoring of four optical fibers (each one with several FBGs available) at a maximum sampling rate of 1 kHz with a sensitivity of 1 $\mu\varepsilon$. Overall, 14 FBGs were attached on several points around the bridge (Figure 3). The spatial extent of the FBGs is 10 mm. The FBG locations are symmetric between the north and south sides of the bridge and their absolute positions on the x-axis are recorded in Table 1. FBGs are pasted at the bottom flange of the bridge bottom chord, either on the flange upper side (alongside the continuous Phase-OTDR fiber) or on the lower side (Figure 5). The second position is used for FBGs between two sections of the bridge (FBGs 3, 5, 10, and 12), which allows sensing the strain in the connecting element of the two sections. The FBG signals are converted to microstrain measurements via the strain constant provided for each FBG by the manufacturer.

2.4.2. Phase-OTDR. Phase-OTDR systems use pulses of highly coherent light, introduced in a sensing optical fiber, to generate Rayleigh backscattering, a small light signal that is correlated to the state of the fiber. Any fiber change (due to strain or temperature perturbations of the structure that the fiber monitors) produces a change in the collected backscattered signal, which allows tracking of the perturbation location and its spectral characteristics. Due to their high sensitivity to vibrations at acoustic frequencies and above, Phase-OTDR systems are also known as distributed acoustic sensors (DAS).

Figure 6 shows the Phase-OTDR interrogation system recently developed by our group [34]. In this system, the laser provides continuous-wave light (1550 nm wavelength) that is pulsed by a semiconductor optical amplifier (SOA), used as a shutter to stimulate the Spectral Hole Burning (SHB) phenomenon. The pulse duration is 50 ns and the pulse repetition rate 500 Hz. The erbium-doped fiber amplifier (EDFA) provides the final amplification to reach a laser peak pulse power of ~400 mW. The circulator directs the laser beam into the fiber under test and the backscattered signal from the fiber to the detection unit, which is then converted to a voltage by the transimpedance amplifier (TIA). The analog-to-digital converter (ADC) digitalizes the analog signal of each trace and sends it to the computer through the USB3 bus. The ADC has an arbitrary signal generator that works as a trigger for the electrical pulse generator of the SOA.

The system is employed in this study for the characterization of the model bridge dynamic behaviour. Despite the limited length of the bridge, this nonlinear Phase-OTDR system can provide meaningful information about separate perturbations by frequency analysis. Indeed, in the study presented below, the Phase-OTDR system provided meaningful spectral content for condition discrimination in a very similar way to FBG sensors. Due to low-cost constraints, the system developed in this work cannot produce in most cases a linear relationship between the perturbation (strain or temperature) and the changes of the backscattered signal, except for very small perturbations.

As shown in Figure 3, there are 14 FBGs installed on the bridge, along with a continuous 80 m standard fiber for the Phase-OTDR system, which senses the entire length of both sides of the bridge. The continuous fiber is glued at the bottom of the base of the lower rods of the bridge both for the north and south sides (Figure 7), while the 68 m long buffer coil of fiber increases the degree of separation between the two bridge sides to avoid signal overlapping.

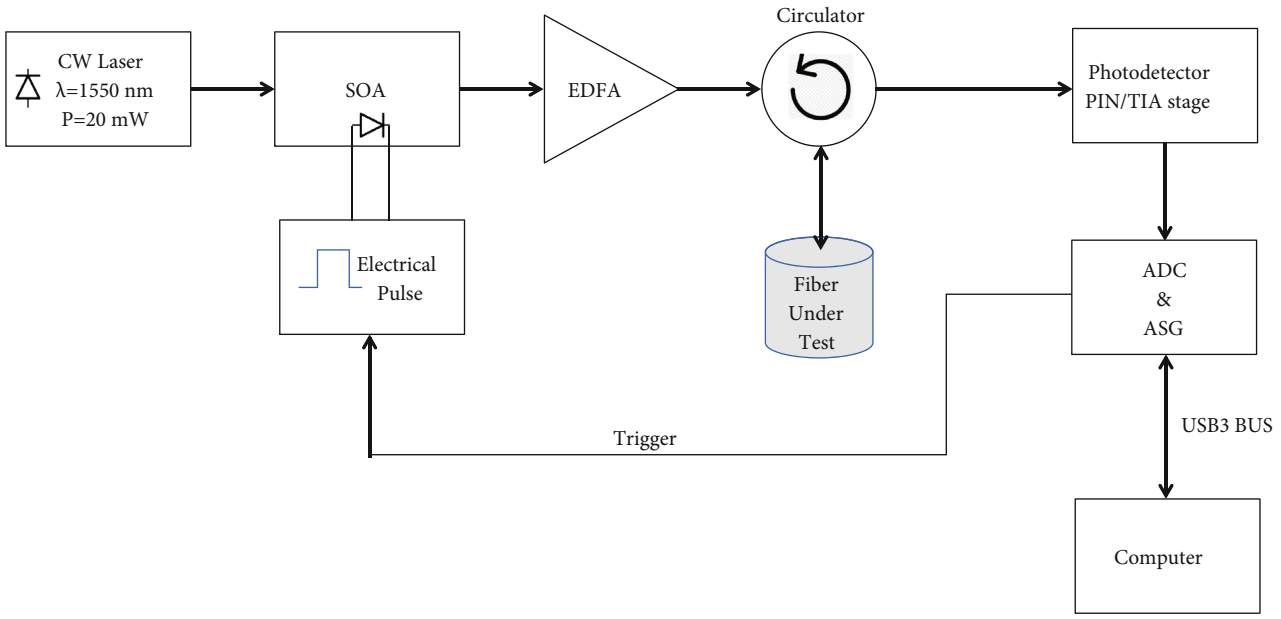

Figure 6: The optoelectronic scheme of the Phase-OTDR developed for this application [33].

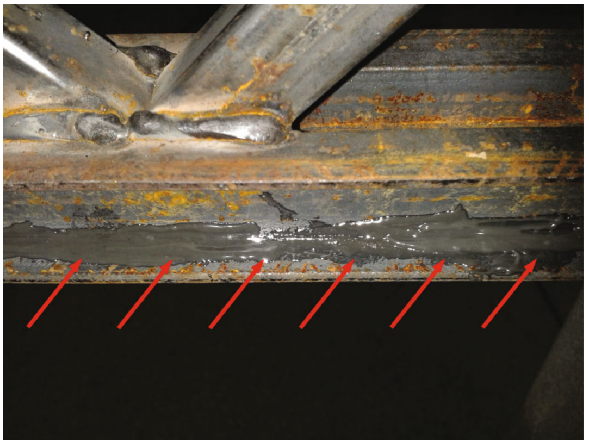

Figure 7: The continuous Phase-OTDR fiber attached to the bottom beam of the bridge, as indicated by the arrows.

2.5. The Laser Tracker System. An additional monitoring system used in the test setup is a laser tracker (LT), as shown in Figure 8. The LT utilizes an extremely high-accuracy distance meter, which is combined with two angle encoders for measuring the elevation and rotational angles and permits the 3D position determination of a retroreflector, which the tracker sensor is continuously tracking, thus allowing continuous measurements. The retroreflector is visible in Figure 2(b), where it was positioned near the excitation point.

The laser tracker used in this work is the FARO Vantage model with the following characteristics:

(i) Distance accuracy: 16 μm ± 0.8 μm/m

(ii) Angular accuracy: 20 μm ± 5 μm/m

Figure 8: The FARO vantage laser tracker.

(iii) Sampling rate: 1000 Hz, max

(iv) Range: 60 m, max

The laser tracker computes the 3D displacements (x, y, z) of the retroreflector which is fixed on a selected point on the bridge. During the tests, two such points were chosen on the south side of the bridge: (i) one point at the absolute position of 411.2 cm (near the excitation shaker) and (ii) a second point at 202.4 cm. The laser tracker data, obtained at the first point, allowed for a reliable measure of the effective excitation induced to the bridge, while the data observed at the second

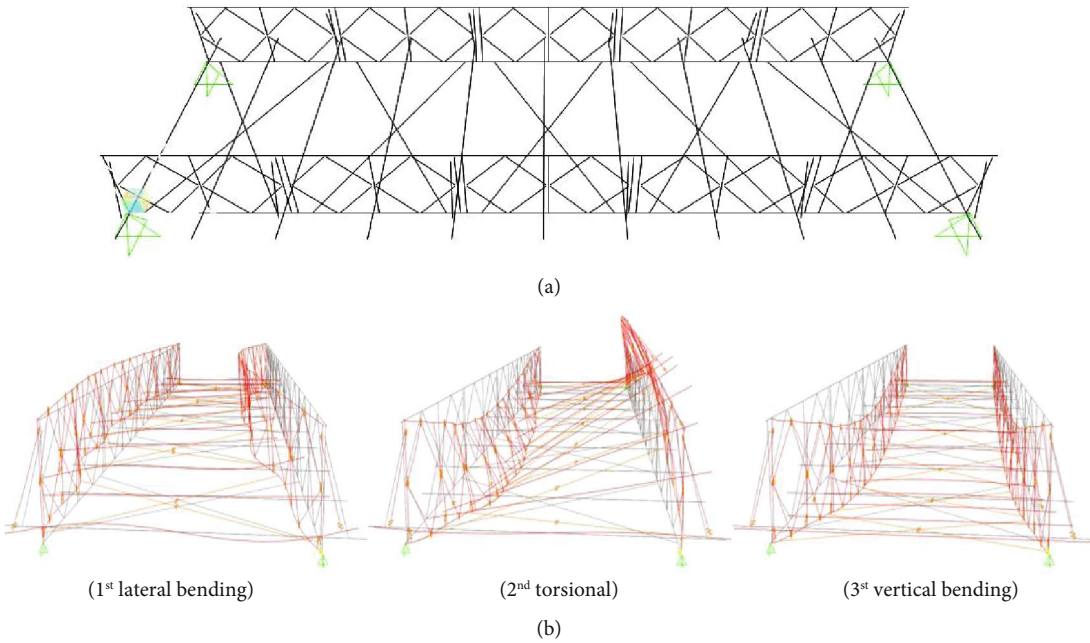

Figure 9: (a) Scaled Bailey bridge FEM model. (b) Eigenmodes obtained from numerical analysis with eigenfrequencies: 1st (lateral bending): $f_{LB,FEM} = 13.09$ Hz; 2nd (torsional): $f_{T,FEM} = 21.24$ Hz; 3rd (vertical bending): $f_{VB,FEM} = 21.85$ Hz.

point allowed the observation of the free movement of this point with respect to the floor.

2.6. Positioning of Sensors. The fiber deployed for the Phase-OTDR system is attached along the entire length of the bridge along the south and north sides. The other three point sensors are dispersed on the bridge, sometimes on the same sensing points to provide a correlation between signals. The FBGs share locations with the Phase-ODTR fiber. Two GBRI corner reflectors were placed near two FBGs (FBG2 = CR3, FBG7 = CR7). FBG9 and FBG14 are located on the south side, symmetrically to FBG2 and FBG7 on the north side. Finally, the laser tracker reflector was positioned during some tests near the excitation shaker rod and on others on a free-moving point.

3. Results and Discussion

3.1. Finite Element Method (FEM) Modelling and Results. In order to evaluate numerically the dynamic characteristics of the scaled bridge model (Figure 9(a)), a FEM model has been developed in the software Sap2000. All members have been simulated as beam finite elements and have been assigned the same section properties as in the physical model. Moreover, material properties assigned to each member are the ones corresponding to structural steel S235, with modulus of elasticity $E = 210$ GPa and specific weight of 7.85 kN/m^3.

All connections at panel members have been assumed to be continuous, as in both the actual bridge and in the scaled physical model the corresponding joints are welded. The panels at each girder are joined together with pins at four corner holes (Figure 1(c)). At these points, rotational releases have been introduced in the FEM model about an axis perpendicular to the girders. The four-point supports have been assumed as hinged.

An eigenvalue analysis has been carried out, and the scaled bridge eigenmodes and corresponding natural frequencies have been extracted. The 1st eigenmode is associated with lateral bending and occurs at $f_{LB,FEM} = 13.09$ Hz,

Table 2: Summary of applied tests.

Test number	Excitation type	LT position	Simulated damage
1	1 Hz	Position 1	No
2	7.4 Hz	Position 1	No
3	23 Hz	Position 1	No
4	1-10 Hz sweep	Position 1	No
5	5-50 Hz sweep	Position 1	No
6	White noise	Position 1	No
7	Shock	Position 1	No
8	1 Hz	Position 2	No
9	7.4 Hz	Position 2	No
10	23 Hz	Position 2	No
11	1-10 Hz sweep	Position 2	No
12	5-50 Hz sweep	Position 2	No
13	White noise	Position 2	No
14	23 Hz	Position 2	No
15	White noise	Position 2	No
16	White noise	Position 2	Center north
17	White noise	Position 2	Shaker south
18	23 Hz	Position 2	Shaker south

LT: laser tracker.

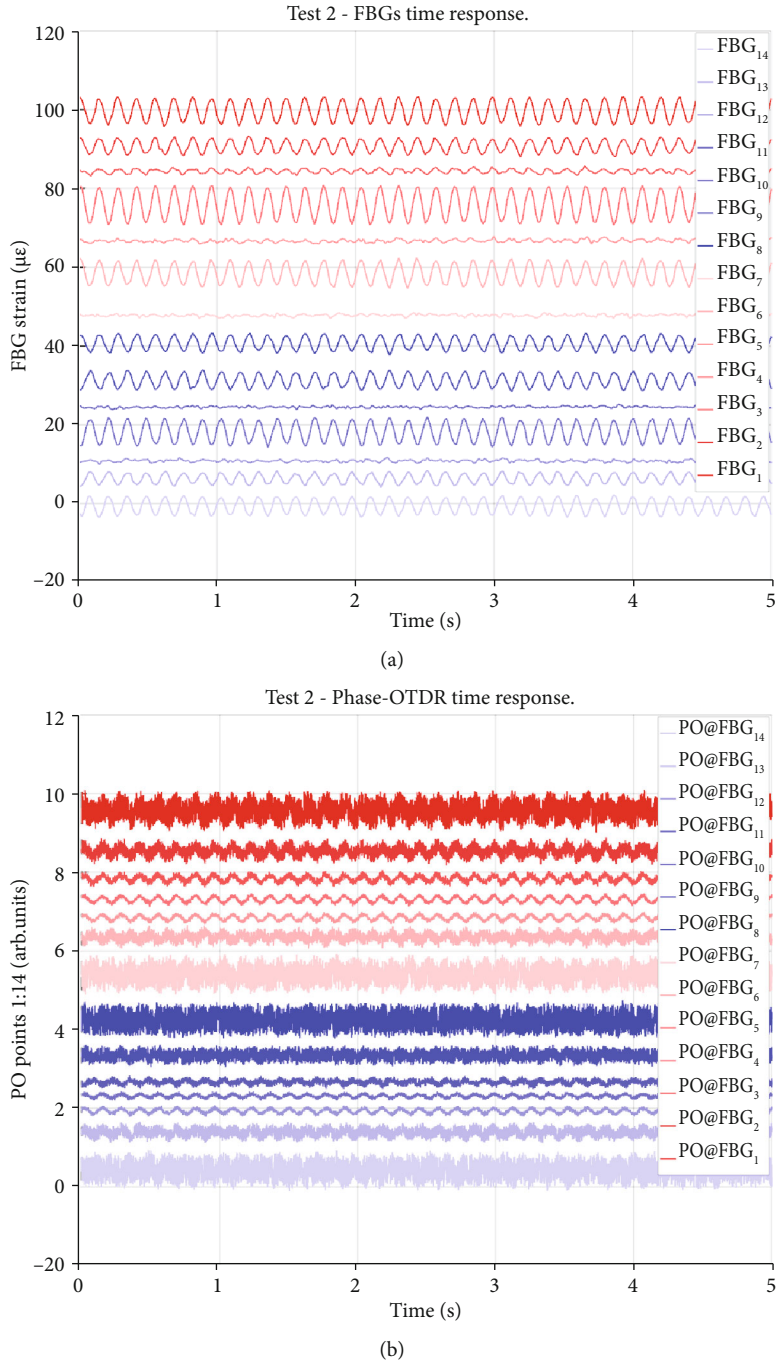

Figure 10: (a) Time response of the 14 FBGs during test 2 (low intensity, single harmonic excitation at 7.4 Hz); blue colour denotes FBGs on the north side of the bridge and red FBGs on the south side. (b) Time response of the Phase-OTDR (PO) system at the locations of the 14 FBGs; in blue are the signals from the north side of the bridge and in red are the signals from the south side.

the 2nd one is torsional at $f_{T,FEM} = 21.24$ Hz, and the 3rd one is characterized by vertical bending at $f_{VB,FEM} = 21.85$ Hz. The eigenmodes and eigenfrequencies obtained from FEM analysis are shown in Figure 9(b).

3.2. Bridge Monitoring. The calculated vertical bending eigenfrequency $f_{VB,FEM}$ was used in order to set an approximate value of vertical excitation at $E_{VE} = 23$ Hz, while lateral and torsional excitations were not systematically studied in this study. Additionally, another set of experiments with excitation frequency at $E_{IMP} = 7.4$ Hz was considered in the study, and despite the fact that the 7.4 Hz frequency was not related to any calculated eigenfrequency, it was empirically identified to be related to some imperfections (such as at the connections) of the physical bridge model that could not be incorporated in the modelling study and captured by FEM analysis. This frequency, attributed to possible

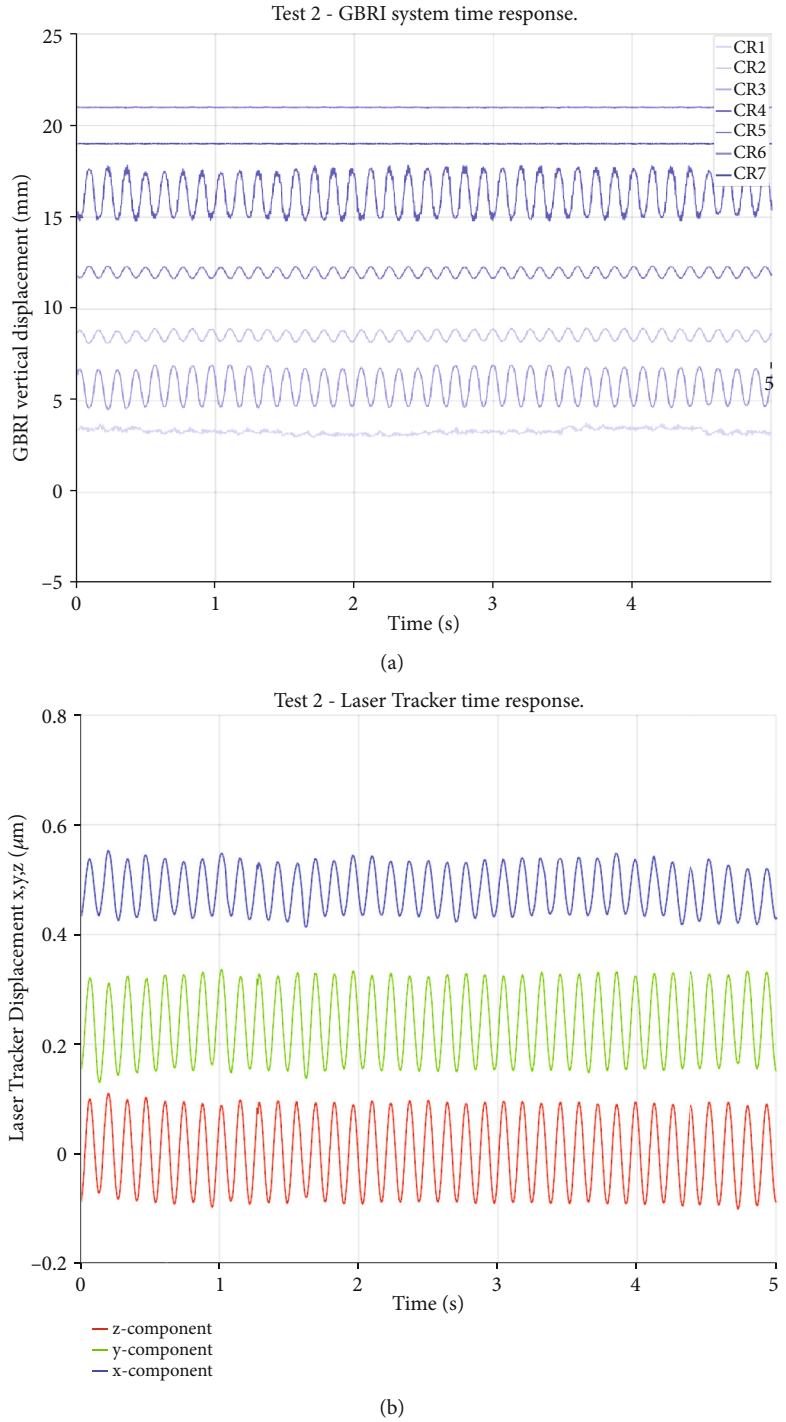

Figure 11: (a) Vertical displacement of the bridge, revealed by the GBRI CRs, positioned on the north side of the bridge. (b) Time response of the LT. x, y, and z directions are defined in Figure 3.

imperfections, will be denoted as f_{IMP}. The experimental analysis below will reveal the good agreement of the vertical bending eigenfrequency $f_{\mathrm{VB,FEM}}$ to the dominant experimentally obtained frequency at ~23 Hz.

We performed 18 tests, summarized in Table 2. The tests can be divided into four categories, depending on the excitation: (a) single harmonic (1 Hz, 7.4 Hz, and 23 Hz), (b) harmonic sweep (1-10 Hz and 5-50 Hz), (c) shock, and (d) white noise. The tests are also divided in two series: in the first series (tests 1 to 7), the LT is in position 1 (411.2 cm, near the excitation shaker on the south side) and the amplitude of the shaker excitation is lower; in the second series (tests 8-18), the LT is in the second position (202.4 cm on the south side) and the amplitude of the shaker

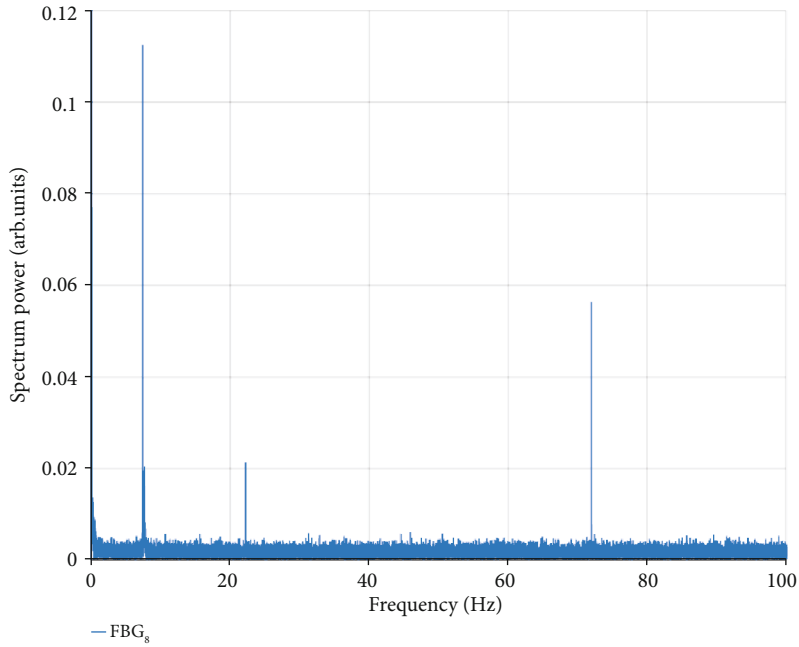

Figure 12: Spectral response of a weak signal in test 2 (FBG8).

excitation is higher. Tests 16–18 intend to show the response of the different technologies to simulated bridge damage. The description of the different damages and results is provided in Section 3.3. Repetition of some tests allows for repeatability check.

Figures 10 and 11 show the retrieved time response for test 2 for FBGs, Phase-OTDR, GBRI, and LT systems; the signals are plotted with a vertical offset for clarity. We deliberately chose test 2 as an example because it was conducted with very low excitation amplitude, to demonstrate the response of the employed technologies to weak input signals. In Figure 10(a), the blue colour is used for FBGs on the north side of the bridge, while the red for the south side. The FBGs between bridge sections (FBG3, FBG5, FBG10, and FBG12) collected a lower signal since they measure strain on a junction. Since a junction can rotate partially, it is likely that these FBGs do not reveal bending and shear stress but they can still measure compression and tension along the longitudinal axis. The other FBGs, which are not located on bridge junctions, tend to provide a measurement in which bending dominates other stresses. The colour pattern is the same in Figure 10(b), which shows the Phase-OTDR signal retrieved for the bridge positions corresponding to the FBGs.

Figure 11(a) shows the vertical displacements reduced from the raw (line-of-sight) displacements at the CR locations using the GBRI system. As expected, the amplitude of displacement is higher towards the center of the bridge span, compared with the bridge anchor points. This observation is in agreement with the displacements detected using the FBG system discussed previously (see Figure 10(a) and 10(b)), keeping in mind that FBGs on bridge junctions collect lower signals due to the junction response. Figure 11(b) shows the 3D displacement components observed by the LT system at the retroreflector target, which is positioned near the excitation shaker (south side). Overall, these results agree with those obtained from the GBRI and FBG systems suggesting a proper function of all observation systems.

As it is shown in Figures 10(a), 10(b), and 11(a), sometimes, the time response signals appear weak, but even these signals carry enough spectral information for a reliable SHM analysis which is true especially for highly sensitive optical sensors. Indeed, in Figure 12, we show the spectral analysis for a weak signal (FBG8), which, not only contains the input excitation signal ($E_{\mathrm{IMP}} = 7.4$ Hz) and the vertical bending eigenfrequency ($f_{\mathrm{VB}} = 22.2$ Hz) but also reveals the presence of a possible higher eigenfrequency (at 72 Hz), even in such critical conditions. On the other hand, other technologies performed less effectively for very weak signals, being unable, for example, to reveal the vertical bending eigenfrequency $f_{\mathrm{VB,FEM}}$ in the same experiment in most cases. Such a result demonstrates that FBG technology is particularly suited for SHM when single-point monitoring is required. Indeed, FBGs are in strict contact with the structure, and they can reveal a practically direct measure, which is mediated only by the glue strain transfer function [21]. Here, we assume a glue strain transfer function of 100%. The noise level in Figure 12 arises mostly from the interrogator and is mainly attributed to the rigidity of the bridge, which results in small values of strain. Optical signals are inherently noisier due to their high bandwidth. Nevertheless, we can clearly identify the spectral content of this signal above the noise level. Graph 12 and also all the following graphs of spectral power distribution are presented dimensionless (by normalizing to the specific units in each graph) in order to homogenize the way of interpretation, since their comparison will be based only on the detected frequency peak position and also to their relative spectral power magnitude.

Table 3: The dominant frequencies revealed by each technology: PO (Phase-OTDR), FBG, GBRI, and LT. Bold values: frequencies common to all the sensors of the same technology; nonbold values: weak frequency signals, present in many but not all sensors of a technology; values in square brackets: correspond to the excitation frequencies and, therefore, are expected; values in parenthesis: frequencies that appear only for certain technologies and are related to the method used.

Excitation	Test #	Dominant frequencies revealed [Hz]
1 Hz No damage	1 LT pos. 1	PO: [**1**], **72** FBG: [**1**], **72** GBRI: [**1**], (**9.5**, 25, **50**), **72**, (**90.6**) LT: [**1**]
	8 LT pos. 2	PO: [**1**], **72** FBG: [**1**], **72** GBRI: [**1**], (**9.5**, **50**), 72, (**90.6**) LT: [**1**], **51.6**
23 Hz	3 no damage LT pos. 1	PO: [**23**], **46**, 66, **69**, **72**, 89, **92**, **112**, **115** FBG: [**23**], **46**, 66, **69**, **72**, 89, **92**, **112**, **115** GBRI: (**9.4**), [**23**], **46**, (50), **69**, (**90.6**) LT: [**23**], **46**, **69**
	10 no damage LT pos. 2	PO: 7.7, 15.3, [**23**], **46**, **69**, **72**, **92**, **112**, 115 FBG: 7.7, 15.3, [**23**], **46**, **69**, 72, **92**, **112**, **115** GBRI: 7.7, **15.3**, [**23**], **46**, (50), **69**, (**90.6**) LT: 7.7, 15.3, [**23**], 46, **69**
	14 no damage LT pos. 2	PO: 11.5, [**23**], **34.5**, **46**, 57.5, 66, **69**, 89, **92**, **112,** 115 FBG: 11.5, [**23**], 34.5, **46**, 57.5, 66, **69**, 89, **92**, **112**, **115** GBRI: 11.5, [**23**], 34.5, 46, (90.6) LT: 11.5, [**23**], **46**, **69**
	18 damage shaker south LT pos. 2	PO: [**23**], **46**, 66, **69**, 72, 89, 92, 112 FBG: 20, [**23**], **46**, **66**, **69**, 72, **89**, **92**, 112 GBRI: (9.4), 21.5, [**23**], 46, **69**, (**90.6**), 92 LT: [**23**], **46**
White noise	6 no damage LT pos. 1	PO: 24, **72** FBG: **23**, **24**, **72** GBRI: (**9.5**, **25**, **50**, **90.6**) LT: **7.6**, (**9.5**), **14.2**, **24**
	13 no damage LT pos. 2	PO: **7.6**, **23**, **24**, **72** FBG: **7.6**, **23**, **24**, **72** GBRI: **7.6**, (**9.4**), **23**, **24**, (**25**, **50**, **90.6**) LT: **7.6**, 24
	15 no damage LT pos. 2	PO: **20.3**, **23**, **24**, **72** FBG: **7.6**, **20.3**, **23**, **24**, **72** GBRI: **7.6**, (**9.5**), **20.3**, **23**, **24**, (**25**, **50**), 81, (**90.6**) LT: **7.6**, (**9.5**), **23**
7.4 Hz No damage	2 LT pos. 1	PO: 1.62, [**7.4**], **72** FBG: [**7.4**], 22.2, **72** GBRI: [**7.4**], (**9.4**), 22.2, (50, **90.6**) LT: [**7.4**], 22.2
	9 LT pos. 2	PO: [**7.4**], 22.2, **72** FBG: [**7.4**], 22.2, **72** GBRI: [**7.4**], (**9.4**, **50**, **90.6**) LT: [**7.4**], (**9.3**)
1-10 Hz sweep No damage	4 LT pos. 1	PO: **7.5**, 14.2, 16, 17.5, **20.5**, **72** FBG: **7.5**, 14.2, 16, 17.5, **20.5**, 72 GBRI: **7.5**, 17.5, **20.5**, (**25**, **50**, **90.6**) LT: **7.5**, **16**, 17.5
	11 LT pos. 2	PO: **7.6**, 16, **17.5**, **20.5**, **72** FBG: **7.6**, 16, 17.5, **20.5**, **72** GBRI: **7.6**, 17.5, **20.5**, (**25**, **50**, **90.6**) LT: **7.6**, **16**, 17

Table 3: Continued.

Excitation	Test #	Dominant frequencies revealed [Hz]
5-50 Hz sweep No damage	5 LT pos. 1	PO: 7.5, **20.5**, **23**, 91.2 FBG: 7.5, **20.5**, **23**, **25**, 91.2 GBRI: 7.5, **20.5**, **23**, **24**, (25, **50**, **90.6)** LT: **7.5**, **16**, **20.5**, **23**
	12 LT pos. 2	PO: **20.3**, 23 FBG: **20.3**, 23 GBRI: 7.5, **(9.4)**, **20.3**, **23**, (25), **44.7**, **(50**, 90.6) LT: **7.5**, **23**
White noise	16 damage 1 center north LT pos. 2	PO: **20.3**, **23**, **24**, **72** FBG: **7.6**, **20.3**, **23**, **24**, **72** GBRI: **7.6**, **(9.5)**, **23**, **24**, **(25**, **50)**, 81, **(90.6)** LT: **7.6**, **(9.5)**, **14**, **16**, **23**, **24**
	17 damage 2 shaker south LT pos. 2	PO: **20.3**, **23**, **24**, **72** FBG: **7.6**, **20.3**, **23**, **24**, **72** GBRI: **7.6**, **(9.5)**, **23**, **24**, **(25**, **50)**, 81, **(90.6)** LT: **7.6**, **(9.5)**, **14**, **16**, **23**, **24**
Shock No damage	7 LT pos. 1	PO: **7.6**, **72** FBG: **7.6**, **72** GBRI: **7.6**, (50, **90.6)** LT: **7.6**

Table 3 and Figure 13 summarize the dominant frequencies in the response of the bridge to the excitation tests described in Table 2, as determined by the distributed Phase-OTDR system (PO) and each of the three commercial point sensor technologies, i.e., FBGs, GBRI, and LT. The tests are grouped to compare those that share similar excitation signals. The frequencies were determined first automatically with a peak detection algorithm and then confirmed manually.

The algorithm was developed and implemented successfully in [40, 41]. As a first step, the algorithm excludes frequencies for which the amplitude is below a certain threshold to remove the noise baseline. The threshold is selected as the noise level in a portion of the spectrum which shows only the baseline noise. Then, it searches for peaks, looking for relative maxima. A linewidth peak is identified if there are no other peaks nearby. The peak value of a wide range harmonic is identified as the central value obtained by weighted averaging. Identifying two peaks as separated depends on the amplitude depression in the valleys of a spectrum between two nearby peaks. The algorithm was fed with the spectral data, as well as threshold and distance values that were set manually and independently for each type of experiment. Depending on the technologies, certain rules were set to define how far away two peaks should be located to be considered as separated. Such a distance is a two-dimension quantity. It is measured on the frequency axis as a number of samples and on the valley between the peaks as its depth with respect to the average value of the two side peaks. The distance is referred to the index difference between discrete indexed frequency peaks. The dominant frequencies are directly identified in harmonic and shock tests, while for white noise and sweep signals, their determination is more complicated.

In Table 3, frequency values in bold are common to all the sensors of the same technology, while nonbold values are weak and present in many but not all sensors. Frequency values in square brackets correspond to the excitation frequencies and, therefore, are expected. Frequency values in parenthesis appear only for certain technologies and are related to the method used. These frequencies in parenthesis appear for all tests with the GBRI method and, in some cases, also for tests with the LT (mostly with white noise excitation). The GBRI data exhibit response signals at 25 Hz and 50 Hz, which might be due to the cross-sensitivity response of the system to the electric power lines. The GBRI system also shows other system-dependent frequencies in parenthesis: 90.6 Hz that is correlated to the CR rod support and 9.3-9.6 Hz, sometimes revealed also by the LT. Since this last value appears for technologies that measure displacement from the floor but does not appear for technologies that measure deformations on the bridge, it is possible that this frequency is related to the support pillars of the bridge. The single harmonic tests are chosen to study the behavior of the bridge at a low excitation frequency (1 Hz) and at the selected excitation frequencies, $E_{IMP} = 7.4$ Hz and $E_{VE} = 23$ Hz.

From Table 3 and Figure 13, we deduce that in general, the instrumented structure demonstrates preferably the eigenfrequency contained in the excitation source; e.g., sweep tests tend to reveal the frequency content f_{IMP} at 7.4 Hz and not $f_{VB,FEM}$ at 21.85 Hz when the sweep is between 1 and 10 Hz, while $f_{VB,FEM}$ appears clearly for sweeps between 5 and 50 Hz. The spectral content changes slightly depending on the technology employed, but fundamental eigenfrequencies are present in all the different monitoring systems, as the captured signals—corresponding to strain or displacement—are linearly related. White noise

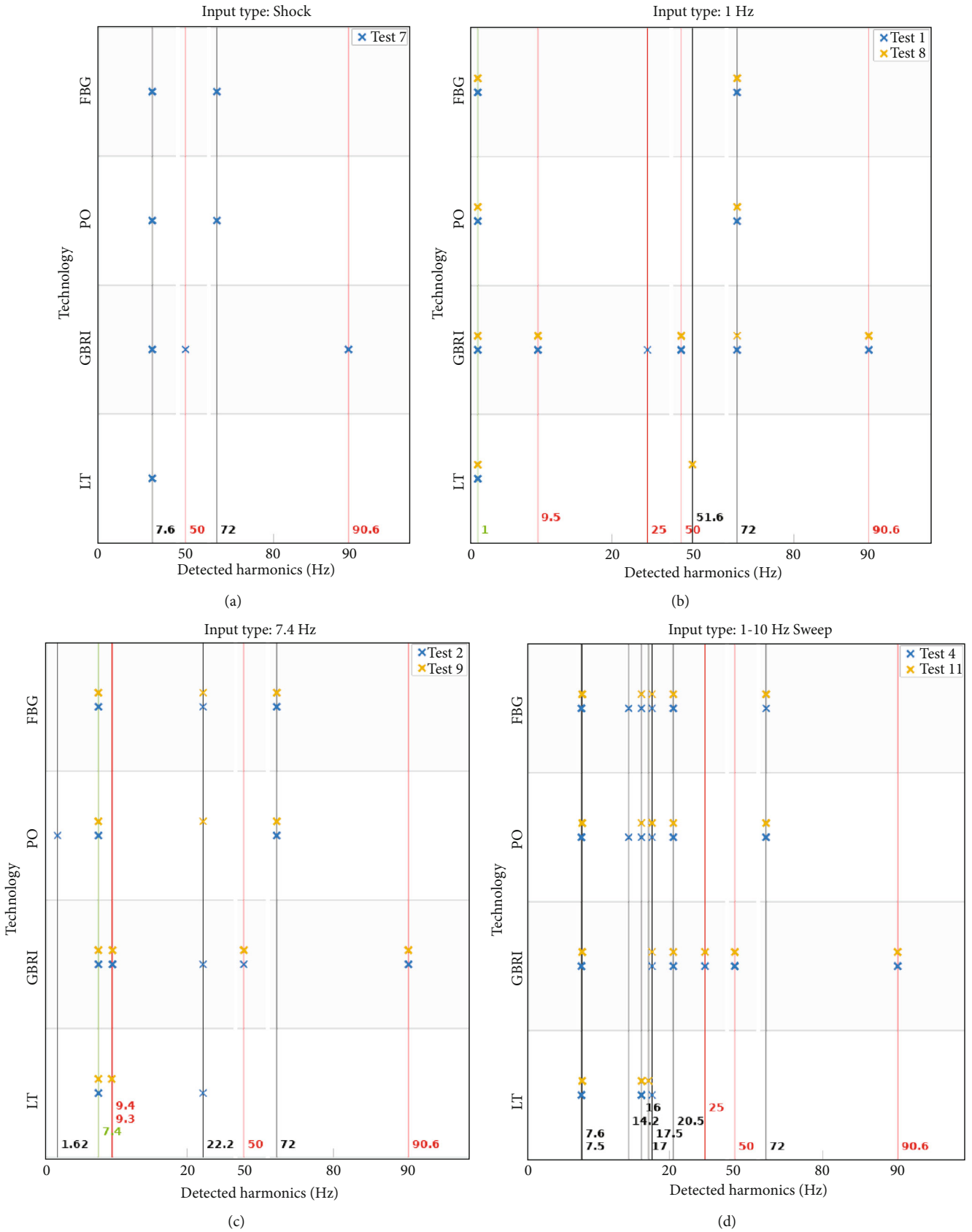

Figure 13: Continued.

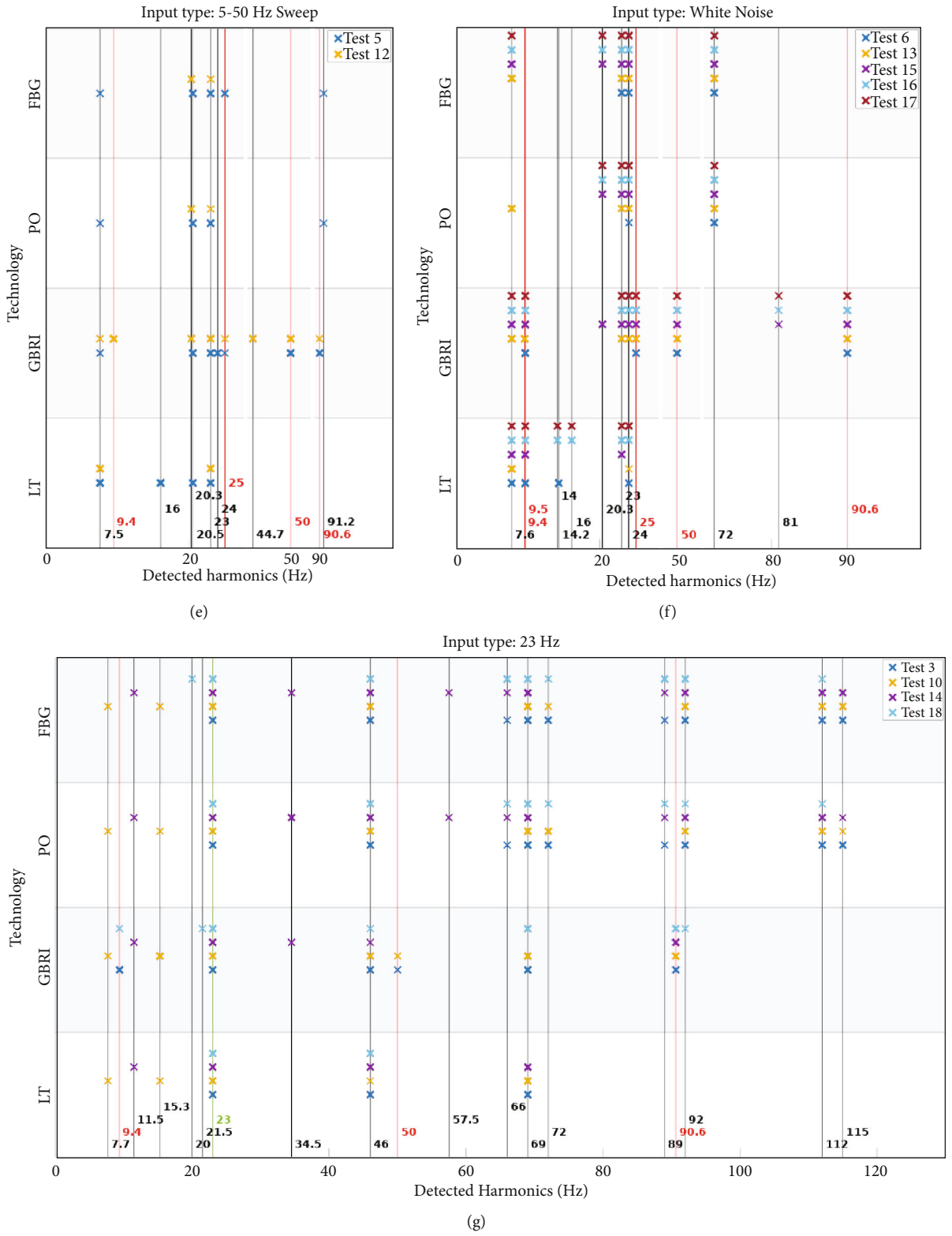

FIGURE 13: The frequencies of the bridge response to different excitation conditions, revealed by the four monitoring systems (PO: Phase-OTDR). Green frequencies are expected to be revealed because they correspond to the excitation frequency. Red frequencies appear only for some, and not all, monitoring technologies. First six graphs have a frequency axis compressed in two points before and after 50 Hz to allow their inline pair fitting.

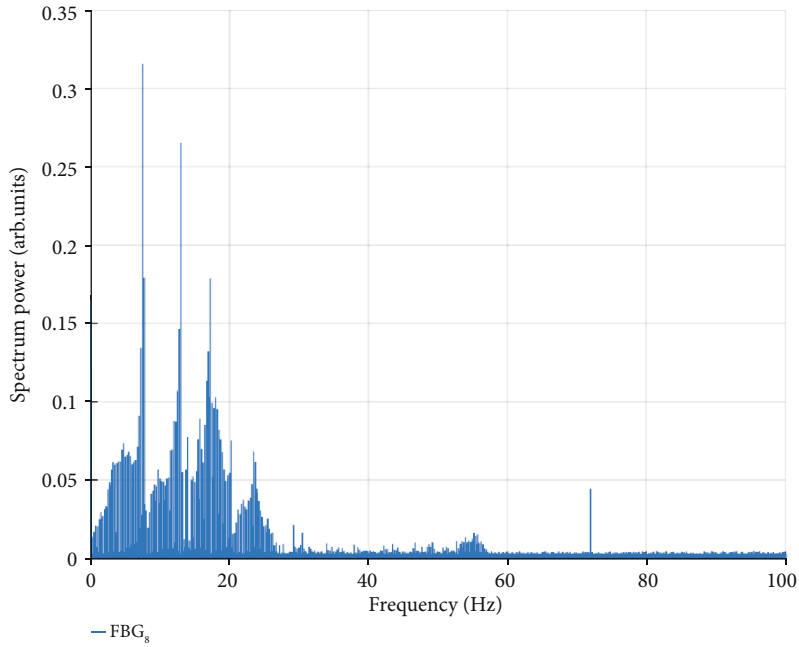

Figure 14: Spectral response of FBG_8 for the sweep input of test 11.

input and, primarily, sweep input tests resulted in a significant number of harmonics present, some of which can be observed for all the sensors of the same technology, while others appear to be partially aleatory.

As it is shown in Figure 14, eigenfrequencies are broadened due to mismatch of the elements constituting the sections of the demountable structure. The effectively obtained frequencies corresponding to eigenfrequencies f_{IMP} and $f_{\mathrm{VB,FEM}}$ are between 7.5 and 7.6 Hz and between 23 and 23.9 Hz, respectively. In Figure 14, we consider the FBG8 sensor again, similar to Figure 12, because it is among the weakest signal FBGs, due to its position near the end of the bridge.

FBG and Phase-OTDR spectral analysis shows that the obtained frequencies corresponding to the vertical bending eigenfrequency $f_{\mathrm{VB,FEM}}$ are higher (blue-shifted) on the south side of the bridge, where the shaker is attached. This shift could be due to the shaker effect or to a mismatch between the supports and the constitutive elements of the bridge. This peculiarity is not yet fully explained based on the available experimental data. Test 7 (shock excitation) revealed the f_{IMP} eigenfrequency content successfully, while it was not adequate to excite the higher vertical bending eigenfrequency $f_{\mathrm{VB,FEM}}$. Single harmonic excitations which match the bridge eigenfrequencies provide responses of higher amplitude. Some eigenfrequencies provide higher response amplitude for structural reasons and high vibration magnitudes, due to nonlinear movements.

Taking advantage of the symmetric form of the model bridge about a vertical plane going through the bridge axis, a useful approach for structure monitoring was also introduced in this study by means of differential response analysis. This analysis is possible when redundant sensors are available: here, sensors at the opposite sides of the bridge are subtracted to highlight differences that correspond to excited modes. In Figure 15, we present an example of this differential analysis for the FBG sensors of test 2. We observe that the sections at the end of the bridge receive lower excitation energy than those at the center (FBG4-FBG11). The FBGs at the junctions of Sections (FBG3, 10) and Sections (FBG5, 12) exhibit lower response signals due to their specific location on points with short leverage.

Despite the clear indications of the effect of FBG positioning relative to the excitation source, the observations cannot be considered as conclusive as there are issues that have not been considered. First, the torsional effects induced by the asymmetric excitation of the structure were not quantitatively considered. Second, construction defects and loose sway brace connections induce a degree of asymmetricity in the bridge, which it was not able to quantitatively justify at a level required for the analysis here.

3.3. Signal Frequency Content Changes Due to Bridge Damage Simulation. Aging changes a structure's dynamic response and condition. Since it is often critical to maintain a certain dynamic response, real-time SHM is usually performed by monitoring the dynamic response during normal operation and during calibrated/well-known excitations (in the case of a bridge, through the passing of known sample vehicles). A modified dynamic response corresponds to a change in the eigenfrequencies and the spectral response of the structure. Therefore, frequency analysis of the dynamic response is a valuable monitoring method for SHM. In this section, we study the effect of structural damage on the spectral content of the response of the bridge and the sensitivity of the different technologies to these spectral changes. The

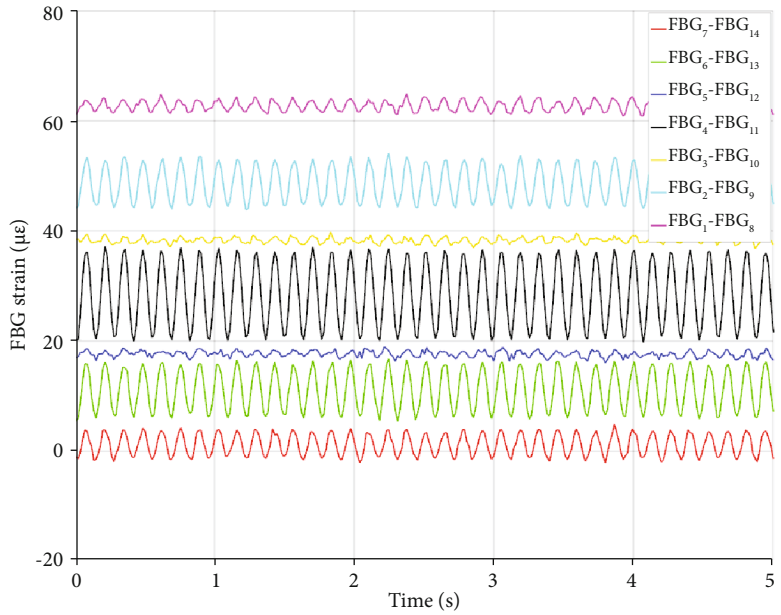

Figure 15: Differential response analysis on the FBGs for test 2.

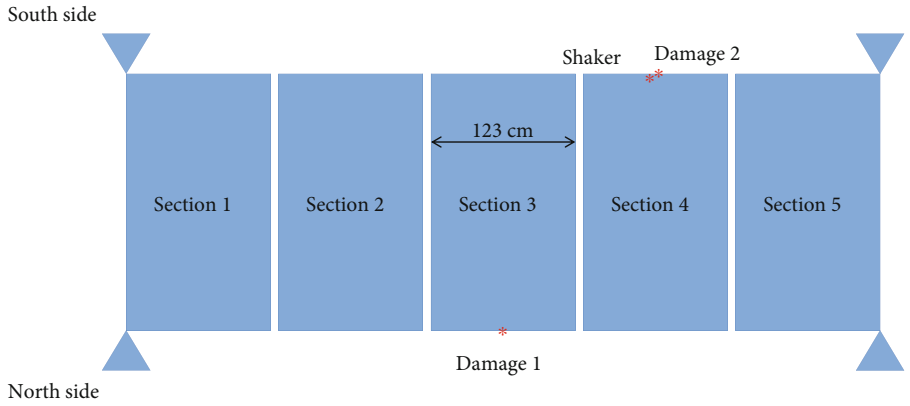

(a)

(b)

Figure 16: (a) Damage locations on the bridge. (b) The centre joining section of the north side of Section 3, which is the position of damage 1.

damage cases we consider are rather simple and correspond to a point defect at a specific known location on the bridge.

Tests 16-18 intend to show the bridge spectral response to two kinds of point defects. According to Figure 16(a), one severe damage (damage 1) is located at the centre of the north side, while one moderate damage (damage 2) is near the shaker (south side). In an operating bridge, fingerprinting is obtained through the passing of a known vehicle

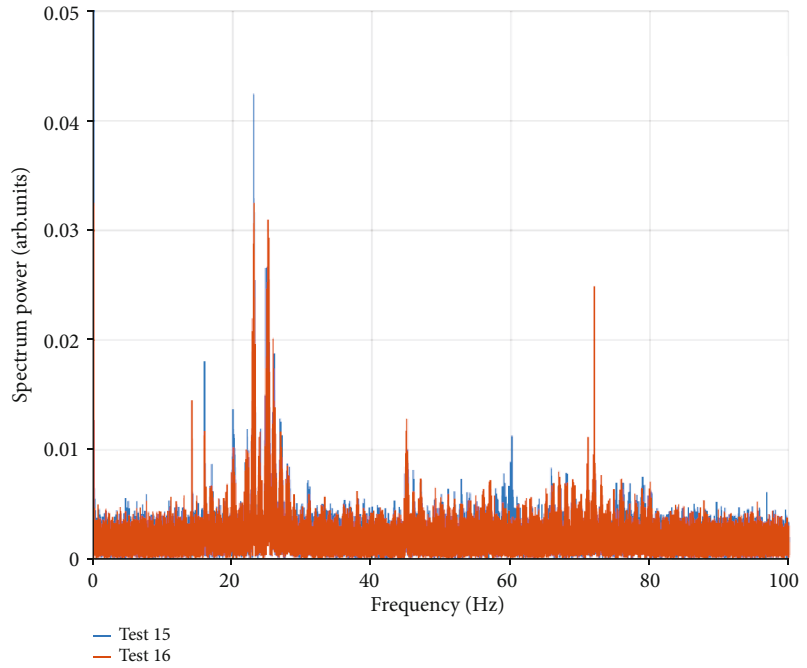

Figure 17: Spectral content change due to damage 1 (test 16 and reference test 15), revealed by FBG13.

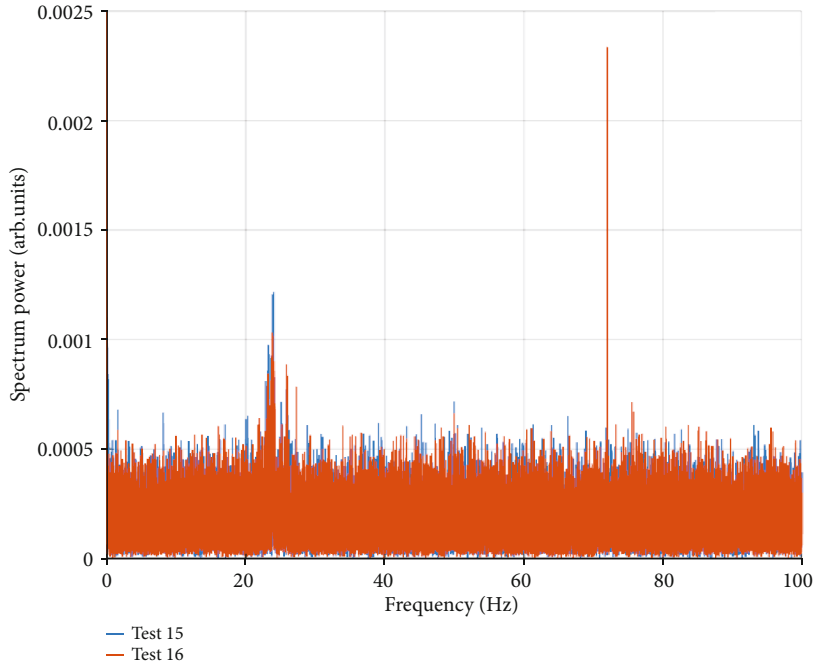

Figure 18: Spectral content change due to damage 1 (test 16 and reference test 15), revealed by the Phase-OTDR system at the location of FBG13.

or persons in pedestrian bridges. In the case of a laboratory test, a valid neutral and reproducible excitation is white noise. The wide bandwidth of white noise assures its neutrality. The first damage was introduced by removing four bolts in a nonwelded joining section on the north side of Section (Figure 16(b)), on the opposite side of the shaker (test 16). The second damage (tests 17 and 18) was a smaller one, consisting of removing only one bolt on a similar joining section (the upper right screw of the centre joining section). The second damage was introduced near the shaker (south side, Section 4). Since the vibrational response of the bridge increases when the distance between damage and excitation source decreases, the second damage could appear like an unrealistic case. However, in any real scenario, every

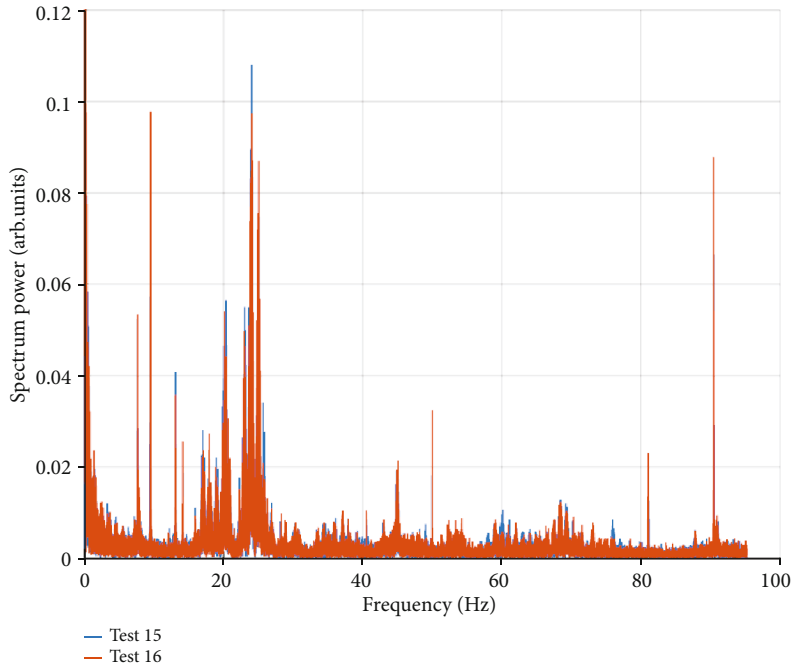

Figure 19: Spectral content change due to damage 1 (test 16 and reference test 15), revealed by CR4.

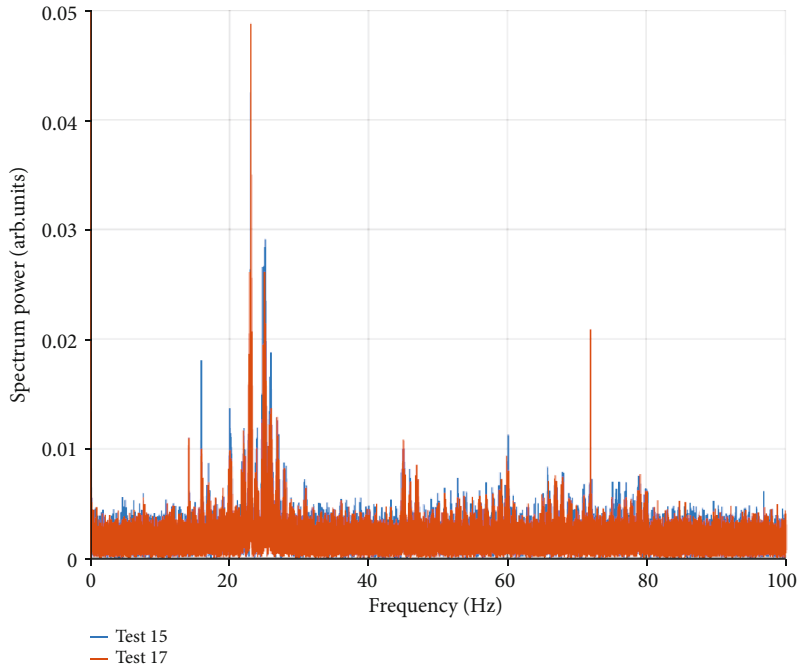

Figure 20: Spectral content change due to damage 2 (test 17 and reference test 15), revealed by FBG13.

bridge-crossing vehicle, sooner or later, passes near the damage, generating a peak in the magnitude of the retrieved data; such a peak corresponds to the second damage study. On the other hand, regarding sensor sensitivity, the first severe damage used for test 16 is a worst-case scenario for successful damage detection because it is relatively far from the excitation source. Indeed, the signals captured by the sensors are almost the same with and without the first damage.

Figures 17–19 show the comparison of spectral analysis for tests 15 and 16 for FBG13, the Phase-OTDR system at the location of FBG13, and CR4, respectively. Test 16 is performed with white noise excitation in the presence of damage 1, and test 15 is the reference white noise excitation without damage. The main changes between the two tests are observed for the bridge eigenfrequency, $f_{\mathrm{VB,\,FEM}}$, around 23 Hz. All three sensors show this peak reduced in intensity

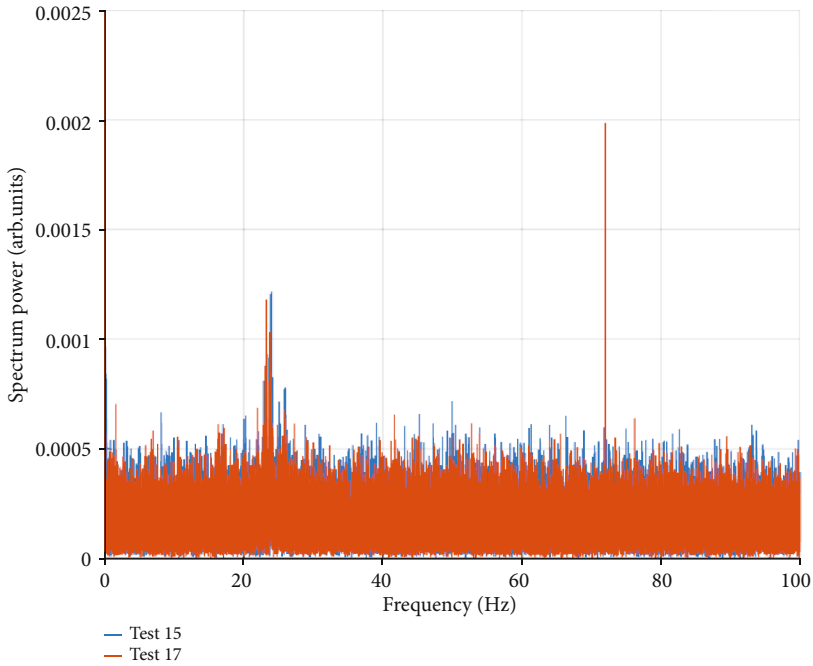

Figure 21: Spectral content change due to damage 2 (test 17 and reference test 15), revealed by the Phase-OTDR system at the location of FBG13.

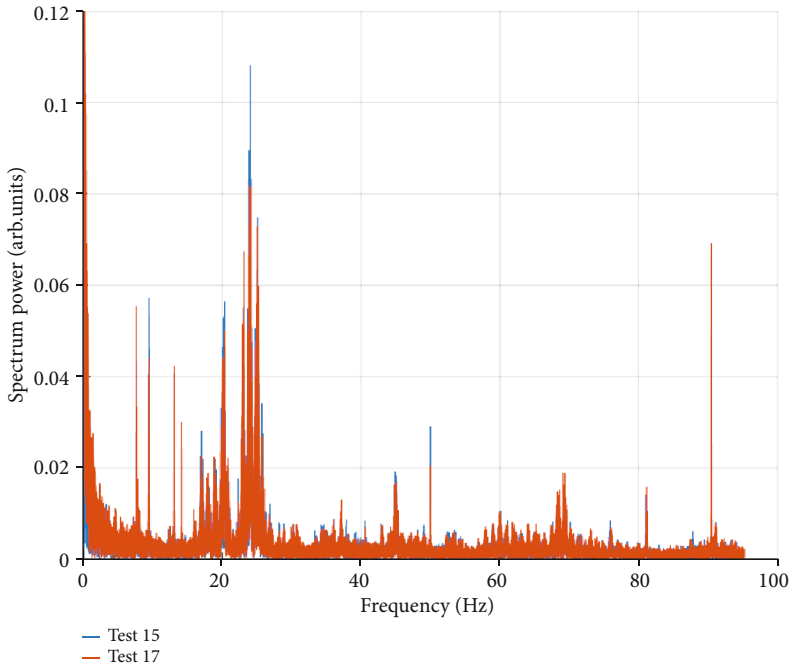

Figure 22: Spectral content change due to damage 2 (test 17 and reference test 15), revealed by CR4.

and blue-shifted by 0.04 Hz as a result of the damage. The two optical sensors, Phase-OTDR and FBGs, also show that a frequency at 72 Hz is pronounced in the case of damage. As we can see in Table 3, this higher-order frequency is not detected by the GBRI system. We note that this nonlinear Phase-OTDR sensor does not relate the linearly strain with the intensity of backscattered light; therefore, the amplitude of the Phase-OTDR spectral lines cannot be compared directly with the amplitude of the FGB spectral lines. However, the line frequency shifts, which indicate a change in the response of the bridge due to the induced damage, are detected by all sensors.

Figures 20 and 21 show the comparison of spectral analysis for tests 15 and 17 for FBG13, the Phase-OTDR system

at the position of FBG13, and CR4, respectively. Test 17 is performed under white noise excitation in the presence of damage 2, and test 15 is the reference test.

Similar to damage 1, the main changes in the presence of damage 2 are observed for the bridge eigenfrequency $f_{VB,FEM}$ and for a higher-order frequency at 72 Hz. However, this time, the $f_{VB,FEM}$ red-shifts by 0.03 Hz due to the effect of damage 2 in the optical fiber sensor signals (Phase-OTDR and FBGs). In the CR4 signal of the GBRI system (Figure 22), we notice a response signal reduction for the vertical bending eigenfrequency $f_{VB,FEM}$. On the other hand, the 72 Hz frequency is pronounced for damage 2 in all three sensor signals.

4. Conclusions

In this work, we demonstrated the simultaneous operation of four minimally invasive and synchronous monitoring techniques for SHM, and we assessed their performance on a scaled steel bridge, a laboratory model of a modular Bailey-type bridge of 1 : 2.5 scale. The experimental validation of a prototype, custom-developed, and low-cost Phase-OTDR fiber system is achieved by implementing, in conjunction, commercial monitoring technologies (FBGs, GBRI, and Laser Tracking). Even though the selected model bridge restricts the characterization of the Phase-OTDR system in the full-scale regime, it provides a useful framework for the collocation and simultaneous operation of three other point-sensing techniques, allowing, in turn, a rigorous correlation and performance characterization of the Phase-OTDR system. In a large-scale infrastructure, this collocation would difficult due to the excessive required number of point sensors.

The experiments were designed in order to excite the natural modes of the bridge. This was achieved by white-noise and sweep sine excitation inputs. Furthermore, we excited the bridge at certain natural frequencies to unveil its reaction in resonance phenomena. The commercial sensors monitor how these excitations manifest themselves in the strain and displacement values of the bridge, and the spectral content of these values is compared to the spectral content of the Phase-OTDR signal, to validate its capability of performing frequency analysis of the dynamic response of a structure. In this approach, all sensors were compared by the obtained spectral response in a unified way. The bridge eigenmodes obtained by FEM analysis of the metallic structure were in close agreement to the fundamental natural frequencies obtained from the bridge excitation and experimental analysis.

As stated earlier, this is not a fully linear Phase-OTDR system, which means it provides linear responses only to small perturbations (i.e., small strain or temperature variation applied to the optical fiber) in contrast to much more expensive and complex interrogation systems. When used with wide signal variations, those systems are nonlinear because there is no track on the previous phase values of the backreflected signal. Several fully linear Phase-OTDR systems have been presented during the last ten years while the commercial systems exhibit a cost much higher than 10 k€ which is the target here. They can be grouped mainly in two categories, compared with the low-cost design presented here:

(a) They need a certain increase of costs on the optical part and a significant increase of cost on the electronic side (doubling photodetector and acquisition system and increasing the required computational power accordingly)

(b) They present increased complexity and costs mainly on the optical part

In both cases, the total system cost increases by a minimum factor of ×5, hindering the device accessibility for applied research and certain field applications. On the other hand, the only parameter that is compromised in the low-cost device shown here is full linearity. The other parameters, such as the dynamic range, bandwidth, and sensitivity, have been optimized as much as possible thanks to a careful choice of components and accurate tuning of the electronics. Given that the system does not have a fully linear response, we demonstrate its application in structural analysis through a frequency content study. A complete discussion on this Phase-OTDR system performance, tuning, cost analysis, and decisions made during its design has been presented in [34], along with several parameter estimations.

The results demonstrate the capability of the truly distributed Phase-OTDR system to provide reliable vibration detection in good agreement with commercial point sensors, such as FBG or GBRI, allowing at the same time the required flexibility and range for applications in large-scale infrastructures. Compared to the other three technologies, the demonstrated Phase-OTDR system with the low-cost customized interrogator system provides a cost-effective technological option per sensed point along km-range lengths. Therefore, this technology applies to several applications requiring long-range SHM, where a large amount of sensors is needed, but point sensors are prohibitive due to their cost.

Data Availability

Data are available on request. The request should be directed to Dr. Massimo Filograno, by email to mfilograno@uj.edu.sa.

Disclosure

Preliminary research results of this work have been presented in the 4th Joint International Symposium on Deformation Monitoring (JISDM 2019), held in Athens, 15–17 May 2019, and were included as unreviewed material in the proceedings of JISDM 2019, as indicated in reference [23].

Conflicts of Interest

The authors declare no conflict of interest.

Acknowledgments

The development and characterization of the prototype Phase-OTDR system presented in this study was funded

from the European Union Horizon 2020 Research and Innovation Programme under the Marie Sklodowska-Curie grant agreement No. 706221.

References

[1] V. Gattulli and L. Chiaramonte, "Condition assessment by visual inspection for a bridge management system," *Computer-Aided Civil and Infrastructure Engineering*, vol. 20, no. 2, pp. 95–107, 2005.

[2] L. Quirk, J. Matos, J. Murphy, and V. Pakrashi, "Visual inspection and bridge management," *Structure and Infrastructure Engineering*, vol. 4, pp. 320–332, 2018.

[3] G. Piniotis, V. Gikas, A. Mpimis, and H. Perakis, "Deck and cable dynamic testing of a single-span bridge using radar interferometry and videometry measurements," *Journal of Applied Geodesy*, vol. 10, no. 1, pp. 87–94, 2016.

[4] V. Gikas, P. Karydakis, A. Mpimis, G. Piniotis, and H. Perakis, "Structural integrity verification of cable stayed footbridge based on FEM analyses and geodetic surveying techniques," *Survey Review*, vol. 48, no. 346, pp. 1–10, 2016.

[5] Z. Chen, X. Zhou, X. Wang, L. Dong, and Y. Qian, "Deployment of a smart structural health monitoring system for long-span arch bridges: a review and a case study," *Sensors*, vol. 17, no. 9, p. 2151, 2017.

[6] X. Ye, X. Chen, Y. Lei, J. Fan, and L. Mei, "An integrated machine learning algorithm for separating the long-term deflection data of prestressed concrete bridges," *Sensors*, vol. 18, no. 11, p. 4070, 2018.

[7] G. M. Calvi, M. Moratti, G. J. O'Reilly et al., "Once upon a time in Italy: the tale of the Morandi bridge," *Structural Engineering International*, vol. 29, no. 2, pp. 198–217, 2019.

[8] V. Zarikas, V. Gikas, and C. Kitsos, "Evaluation of the optimal design "cosinor model" for enhancing the potential of robotic theodolite kinematic observations," *Measurement*, vol. 43, no. 10, pp. 1416–1424, 2010.

[9] V. Gikas, "Smart RTS: monitoring highly dynamic structures," *GIM International*, vol. 22, no. 6, pp. 44-45, 2012.

[10] P. Psimoulis and S. C. Stiros, "Measuring deflections of a short-span railway bridge using a robotic total station," *Journal of Bridge Engineering*, vol. 18, no. 2, pp. 182–185, 2013.

[11] F. Moschas and S. C. Stiros, "Three-dimensional dynamic deflections and natural frequencies of a stiff footbridge based on measurements of collocated sensors," *Structural Control and Health Monitoring*, vol. 21, no. 1, pp. 23–42, 2014.

[12] W. Lienhart, M. Ehrhart, and M. Grick, "High frequent total station measurements for the monitoring of bridge vibrations," *Journal of Applied Geodesy*, vol. 11, no. 1, pp. 1–8, 2017.

[13] V. Gikas, A. Mpimis, G. Piniotis et al., "Long-term monitoring of the tall piers of a girder bridge using a network of digital inclinometers: first results and perspectives for future analyses," in *Proceedings of the 4th Joint International Symposium on Deformation Monitoring (JISDM)*, pp. 15–17, Athens, Greece, 2019, May.

[14] R. Zhang, C. Gao, S. Pan, and R. Shang, "Fusion of GNSS and speedometer based on VMD and its application in bridge deformation monitoring," *Sensors*, vol. 20, no. 3, p. 694, 2020.

[15] C. O. Yigit, A. A. Dindar, A. El-Mowafy, M. Bezcioglu, and V. Gikas, "Investigating the ability of high-rate GNSS-PPP for determining the vibration modes of engineering structures: small scale model experiment," in *Proceedings of 4th Joint International Symposium on Deformation Monitoring*, pp. 15–17, Athens, Greece, 2019, May.

[16] J. Yu, X. Meng, B. Yan, B. Xu, Q. Fan, and Y. Xie, "Global navigation satellite system-based positioning technology for structural health monitoring: a review," *Structural Control and Health Monitoring*, vol. 27, no. 1, pp. 1–27, 2020.

[17] V. Gikas, "Ambient vibration monitoring of slender structures by microwave interferometer remote sensing," *Journal of Applied Geodesy*, vol. 6, no. 3-4, pp. 167–176, 2012.

[18] J. J. Lee, H. N. Ho, and J. H. Lee, "A vision-based dynamic rotational angle measurement system for large civil structures," *Sensors*, vol. 12, no. 6, pp. 7326–7336, 2012.

[19] I. R. Matias, S. Ikezawa, and J. Corres, *Fiber optic sensors: current status and future possibilities, smart sensors, measurement and instrumentation*, Springer, 2017.

[20] A. Barrias, J. R. Casas, and S. Villalba, "A review of distributed optical fiber sensors for civil engineering applications," *Sensors*, vol. 16, no. 5, p. 748, 2016.

[21] H. Wang, P. Xiang, and L. Jiang, "Strain transfer theory of industrialized optical fiber-based sensors in civil engineering: a review on measurement accuracy, design and calibration," *Sensors and Actuators A: Physical*, vol. 285, pp. 414–426, 2019.

[22] V. Pruneri, C. Riziotis, P. G. R. Smith, and A. Vasilakos, "Fiber and integrated waveguide-based optical sensors," *Journal of Sensors*, vol. 2009, Article ID 171748, 3 pages, 2009.

[23] M. L. Filograno, G. Piniotis, V. Gikas et al., "Experimental validation of a prototype photonic phase optical time domain reflectometer for SHM in large-scale infrastructures," in *4th Joint International Symposium on Deformation Monitoring (JISDM)*, Athens, Greece, 2019.

[24] P. Lu, N. Lalam, M. Badar et al., "Distributed optical fiber sensing: review and perspective," *Applied Physics Reviews*, vol. 6, no. 4, article 041302, 2019.

[25] P. Xiang and H. Wang, "Optical fibre-based sensors for distributed strain monitoring of asphalt pavements," *International Journal of Pavement Engineering*, vol. 19, no. 9, pp. 842–850, 2018.

[26] J. M. Lopez-Higuera, L. Rodriguez Cobo, A. Quintela Incera, and A. Cobo, "Fiber optic sensors in structural health monitoring," *Journal of Lightwave Technology*, vol. 29, no. 4, pp. 587–608, 2011.

[27] Z. He, Q. Liu, X. Fan, D. Chen, S. Wang, and G. Yang, "A review on advances in fiber-optic distributed acoustic sensors (DAS)," in *Proceedings CLEO Pacific Rim Conference*, p. Th2L.1, Hong Kong, China, 2018.

[28] Y. Muanenda, "Recent advances in distributed acoustic sensing based on phase-sensitive optical time domain reflectometry," *Journal of Sensors*, vol. 2018, Article ID 3897873, 16 pages, 2018.

[29] A. Masoudi and T. P. Newson, "Analysis of distributed optical fibre acoustic sensors through numerical modelling," *Optics Express*, vol. 25, no. 25, pp. 32021–32040, 2017.

[30] J. Tejedor, J. Macias-Guarasa, H. F. Martins et al., "Towards detection of pipeline integrity threats using a smart fiber-optic surveillance system: pit-stop project blind field test results," in *25th International Conference on Optical Fiber Sensors*, Jeju, Korea (South), 2017.

[31] M. G. Shlyagin, A. Arias, and R. Martinez Manuel, "Distributed detection and localization of multiple dynamic perturbations using coherent correlation OTDR," in *23rd International Conference on Optical Fibre Sensors. Vol. 9157. International Society for Optics and Photonics*, Santander, Spain, 2014.

[32] J. Pastor-Graells, H. F. Martins, A. Garcia-Ruiz, S. Martin-Lopez, and M. Gonzalez-Herraez, "Single-shot distributed temperature and strain tracking using direct detection phase-sensitive OTDR with chirped pulses," *Optics Express*, vol. 24, no. 12, pp. 13121–13133, 2016.

[33] H. F. Martins, S. Martin-Lopez, P. Corredera, M. L. Filograno, O. Frazao, and M. Gonzalez-Herraez, "Coherent noise reduction in high visibility phase-sensitive optical time domain reflectometer for distributed sensing of ultrasonic waves," *Journal of Lightwave Technology*, vol. 31, no. 23, pp. 3631–3637, 2013.

[34] M. L. Filograno, C. Riziotis, and M. Kandyla, "A low-cost phase-OTDR system for structural health monitoring: design and instrumentation," *Instruments*, vol. 3, no. 3, p. 46, 2019.

[35] DOA-Department of the Army, *Bailey Bridges FM5-277*, Headquarters Department of the Army, Washington, DC, USA, 1986.

[36] C. Gentile, *Application of radar technology to deflection measurement and dynamic testing of bridges, radar technology*, G. Kouemou, Ed., InTechOpen, 2010.

[37] M. Pieraccini and L. Miccinesi, "Ground-based radar interferometry: a bibliographic review," *Remote Sensing*, vol. 11, no. 9, p. 1029, 2019.

[38] J. Gocal, L. Ortyl, T. Owerko et al., *Determination of displacements and vibrations of engineering structures using ground-based radar interferometry*, Wydawnictwa AGH, 2013.

[39] M. M. Werneck, R. C. S. B. Allil, B. A. Ribeiro, and F. V. B. de Nazaré, *A guide to fiber Bragg grating sensors*, IntechOpen, 2013.

[40] M. L. Filograno, P. Corredera, M. Rodríguez-Plaza, A. Andrés-Alguacil, and M. González-Herráez, "Wheel flat detection in high-speed railway systems using fiber Bragg gratings," *IEEE Sensors Journal*, vol. 13, no. 12, pp. 4808–4816, 2013.

[41] M. L. Filograno, P. Corredera Guillen, A. Rodriguez-Barrios et al., "Real-time monitoring of railway traffic using fiber Bragg grating sensors," *IEEE Sensors Journal*, vol. 12, no. 1, pp. 85–92, 2012.